Dynamic System for Instability Predictions: A Truss-Braced Aircraft Wing
EME 139 Team Term Paper Final Report

Team Name: A04 Group 3
TP Report #: Final Report
Date: 06/07/2026
Team Members:
Ivan Leung, ivleung@ucdavis.edu
Anthony Damian, agdamian@ucdavis.edu
Elian Castillo, etcastillo@ucdavis.edu
Jacob George, jageorge@ucdavis.edu
Kaitaro Hori, khori@ucdavis.edu

Professor N. Sarigul-Klijn
University of California, Davis
EME 139: Stability of Flexible Dynamic Systems

Table of Contents:

Section 1: System Description, Mission, and Goal of Study

Description of the System:

The system studied in this project is a truss-braced aircraft wing, or TBW. The assigned wing uses a modified Boeing-Vertol VR-7 airfoil with a -3° tab, with the airfoil thickness increased from 12.03% to 14%. The main structural components include the wing skin, internal ribs, aluminum spar, main strut, and jury strut. The spar runs along the span of the wing and acts as the primary load-carrying member, while the strut and jury strut provide additional support and influence the wing's vibration behavior. The assigned geometry includes an 18.14 in chord and a 12.5 ft half-span measured from the wing pivot. The spar and struts are aluminum, while the ribs are ABS plastic. The project guide also lists a 0.140 in skin thickness, 0.10 in ribs spaced every 2.25 in, and a 3 in by 2 in by 1/4 in aluminum spar located 5.442 in aft of the leading edge.

Mission of the System:

The mission of the truss-braced wing system is to provide a lightweight aircraft wing structure that can maintain stability and stiffness while operating in flight. The truss-braced design is useful because the external strut support can increase structural stiffness without relying only on a heavier wing box. For this project, the mission of the model is not to design a complete aircraft, but to study how the wing structure behaves dynamically and how changes in support conditions affect natural frequencies, mode shapes, and aeroelastic stability.

Goal of the Study:

The goal of this study is to model and analyze the dynamic behavior of the assigned truss-braced aircraft wing. The project requires a simplified 1D model, a higher-fidelity Patran/Nastran model, extraction of the first 15 natural frequencies and mode shapes, comparison between the simplified and higher-fidelity models, and an investigation of flutter or divergence behavior under selected operating conditions. The project also asks the team to study how boundary conditions, including the spar, strut, and jury strut configuration, influence the vibration behavior and stability of the system.

Operating Condition:

The assigned operational requirements include a maximum indicated speed of 250 knots, maximum gross weight of 2400 lb, and maximum altitude of 32,000 ft MSL. For the final report, the operational envelope is discussed using flow speed as the main comparison variable because flutter and divergence are aeroelastic instabilities that depend strongly on speed. The project guide also requires solutions at two angles of attack, 6° and 8°, and at least two altitudes, including sea level and one selected altitude between 10,000 ft and 32,000 ft MSL.

Section 2: Model Description, Specifications, and Assumptions

Model Description:

Two main modeling approaches were used for this project. The first approach was a simplified 1D Euler-Bernoulli beam model created to estimate the flapwise bending behavior of the wing using the spar as the main structural member. This model was useful as a first-pass estimate because it gave quick natural frequency results and helped show the effect of adding strut stiffness. The second approach was a higher-fidelity Patran/Nastran model that represented the wing geometry in more detail, including the airfoil shape, spar, ribs, skin, and strut structure. The higher-fidelity model was needed because the simplified 1D model cannot capture torsion, local rib and skin behavior, or full 3D structural coupling.

Specifications:

Parameter	**Value**
Airfoil	Modified Boeing-Vertol VR-7 with -3° tab
Airfoil thickness	Increased from 12.03% to 14%
Wing chord	18.14 in
Wing half-span	12.5 ft, or 150 in
Spar material	Aluminum
Rib material	ABS plastic
Spar size	3 in * 2 in * 1/4 in aluminum tube
Spar centerline	5.442 in aft of leading edge
Rib thickness	0.10 in
Rib spacing	2.25 in
Skin thickness	0.140 in
Main strut width	3 in
Main strut thickness	3/8 in
Main strut wing attachment	6 ft from root
Fuselage attachement	2.5 ft below root
Maximum indicated speed	250 knots

Maximum gross weight	2400 lb
Maximum altitude	32,000 ft MSL

Property	**ABS Plastic**	**Aluminum**
Elastic modulus	200,000 psi	10,000,000 psi
Poisson's ratio	0.35	0.30
Tension stress limit	6,100 psi	40,000 psi
Compression stress limit	7,600 psi	32,000 psi
Shear stress limit	27,000 psi	27,000 psi

Assumptions:
For the simplified model, the wing was treated as a one-dimensional Euler-Bernoulli beam. The aluminum spar was modeled as the main load-carrying member, and the model only captured flapwise bending. The spar was modeled as a 3 in chordwise by 2 in vertical by 1/4 in rectangular aluminum tube. This orientation was chosen because the assigned maximum airfoil thickness is about 2.54 in, so the 2 in vertical spar dimension physically fits inside the airfoil thickness envelope. The simplified model used a 150 in half-span, 200 beam elements, 201 nodes, and an element length of 0.75 in. The finite axial strut support case represented the main strut as an equivalent vertical spring at the strut attachment location.

The simplified model has important limitations. It does not capture torsion, chordwise bending, local rib deformation, skin deformation, joint flexibility, aerodynamic loading, damping, or full 3D coupling. The jury strut was also not modeled as a separate member in the simplified 1D model. Because of this, the simplified model was used as a first-pass comparison tool rather than a final high-fidelity prediction.

Section 3: Tutorial: Steps to Create the Model

Airfoil and Wing Geometry Setup:

The modeling process began by defining the assigned airfoil geometry and overall wing dimensions from the project handout. The airfoil cross-section was created using the modified Boeing-Vertol VR-7 geometry. The wing was modeled with a total span of 150 in, and the repeated rib/spar/skin blocks were arranged spanwise to match this required dimension.

Because the wing has an angle of incidence of 6°, the main wing structure was first created before adding the strut and jury strut geometry. This made it easier to project the strut attachment points onto the lower surface of the completed wing geometry.

Airfoil Coordinates:

1. Go to an open-source airfoil plotter (http://airfoiltools.com/plotter)

2. Select Boeing-Vertol VR-7 airfoil and extract the .txt file of the airfoil.
3. Change the thickness to 116% on Excel to be 14% of the chord.
4. Change the chord to 460.8567 mm.
5. Create z coordinates of 0 for each coordinate.
6. Convert all the entries to inches by dividing by 25.4.

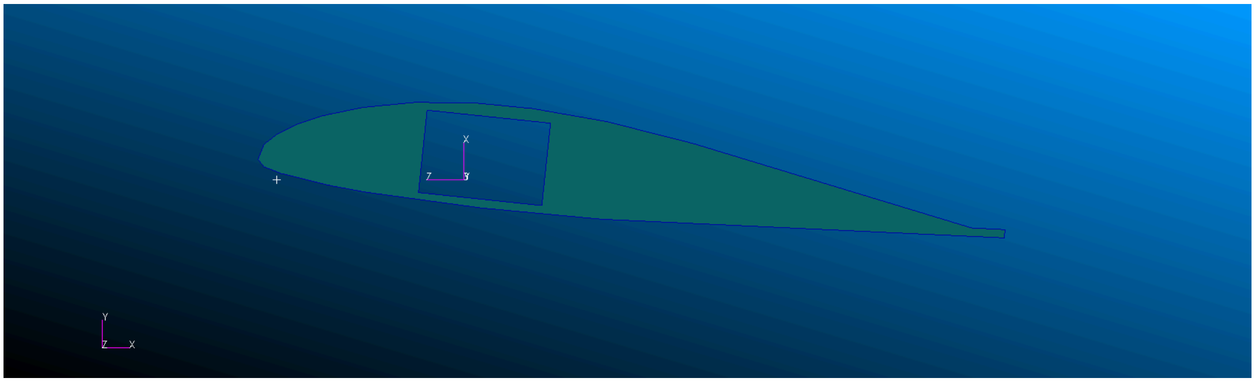

Figure 1: Cross Section of the Rib as a 2D Shell

Rib Modeling:

The rib geometry was created from the assigned airfoil coordinate data. Before importing the geometry into Patran, the airfoil coordinates were adjusted in Excel so that the units and geometry matched the required wing model dimensions. The airfoil coordinate data was organized in an x-y-z format, with the cross-section placed in the x-y plane and z = 0. The final chordwise length of the airfoil section was 18.144 in, which was used as the full chord length for the rib geometry.

After the adjusted airfoil coordinates were prepared, the rib surface was created from the modified airfoil cross-section. This rib geometry included the tab region, allowing the rib shape to match the final wing cross-section used in the model. A cutout was then made in the rib for the outer perimeter of the spar. This allowed the spar to pass through the rib while keeping the rib and spar as separate structural components.

Using the group function in Patran, the ribs were placed into their own group. This allowed the rib material, shell property, mesh, and boundary/connectivity conditions to be assigned separately from the spar, skin, and strut components. Keeping the ribs as a separate group also made it easier to troubleshoot the model and verify that the ribs were properly connected to the spar and skin during the normal mode analysis.

Rib modeling on Patran:

1. On Patran, Create the first and last two points at the leading edge and trailing edge for the upper and lower curve.
2. Create 4 vectors from each pair of points.
3. Create a spline curve for the upper and lower curves from the Excel.
4. Create points at the coordinates [17.32752, 0.156800433070866, 0] [17.32752, -0.048408188976378, 0] to be hinge points for the 3° tab.

5. Break the upper and lower curves with the points defined at the step 7 and connect each hinge point with coordinates [18.14, 0.199380705582751, 0] and [18.14, -0.005827916464493, 0] to make a tab.
6. Close the tab by connecting upper and lower edges.
7. Create a point at a quarter of the chordline [4.536, 0, 0] to rotate the entire rib by -6°.
8. Using the coordinates in **Figure 2A** in the Appendix, create 4 points and 4 curves to cut out the surface for the spar.
9. After making a surface with upper/lower curves and a surface with spar curves, subtract the spar surface from the rib surface, and delete the spar surface to have a cutout rib surface, which should be labeled as Surface 1 as shown in **Figure 1** above.

Spar Modeling:

The spar was modeled using 2D shell elements instead of a 3D solid representation. Since the actual spar has a wall thickness of 0.25 in, the spar shell geometry was created by defining the midline between the outer and inner spar perimeters. This midline was used as the basis for the 2D shell representation of the spar walls.

The spar was also placed into a separate group so that its shell property and boundary conditions could be assigned independently.

Spar Block:

1. Create 4 curves with coordinates shown in **Figure 1A** in the Appendix for the spar.
2. Transform those curves by 2.25 inches.
3. Make connecting curves at each edge and make 4 surfaces.

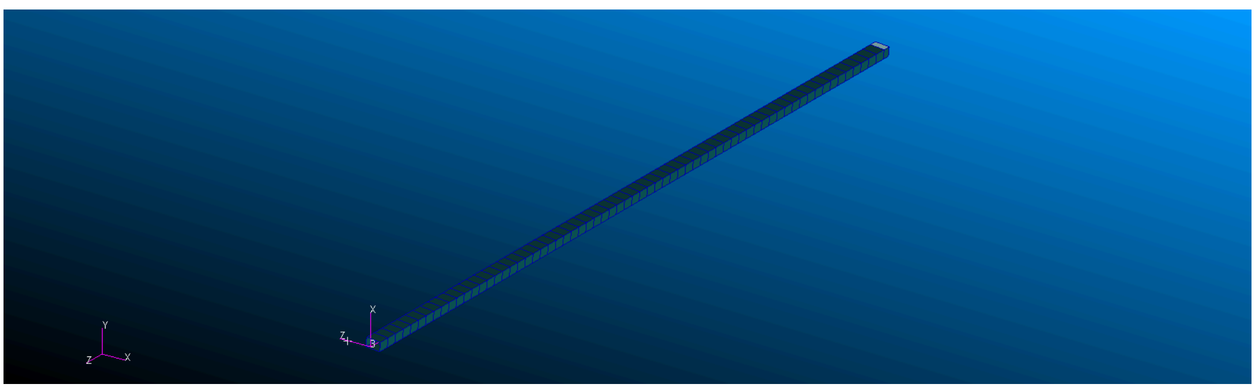

Figure 2: Spar after repeated

Repeating the Rib and Spar Blocks:

After one rib-and-spar block was completed, the block was repeated along the span. This repeated block included the rib surface, spar shell surfaces, and their corresponding grouped geometry. The block was repeated 65 additional times, with the final block spaced 1.5 in apart to fit the full 150-in wing span.

This repeated-block method helped keep the wing geometry consistent and made the model easier to organize in Patran.

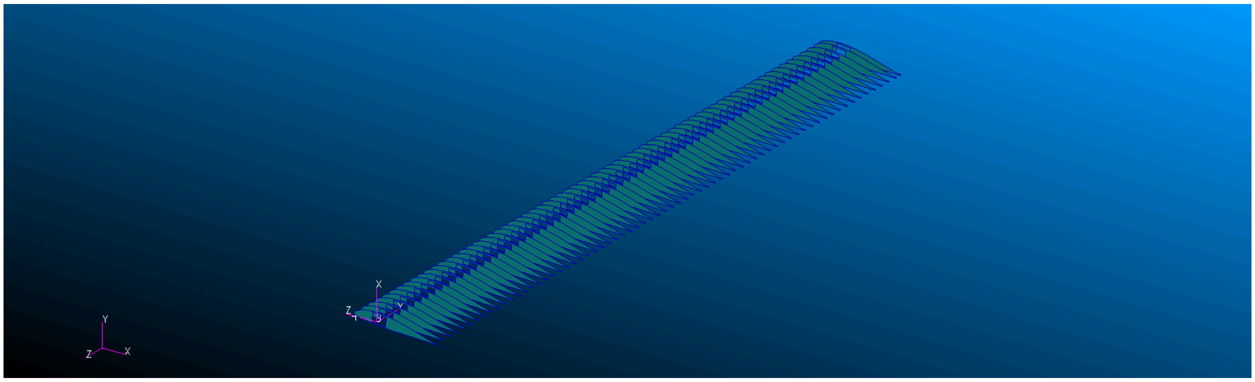

Figure 3: Ribs

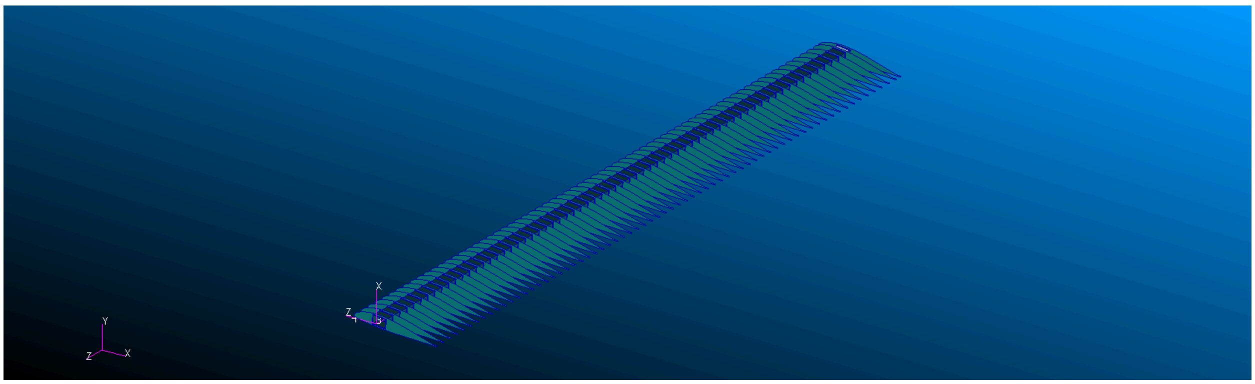

Figure 4: Ribs and Spar

Wing Skin Modeling:

The wing skin was also modeled using 2D shell surfaces. Separate surfaces were created for the upper skin, lower skin, and the closing surface near the tab region. These skin surfaces were created as a block and repeated along the span using the same spacing strategy as the ribs and spar.

The skin was placed into its own group so that the material, shell thickness, and mesh could be assigned separately. Keeping the skin separate also made it easier to check whether the skin was properly connected to the ribs and spar during the modal analysis.

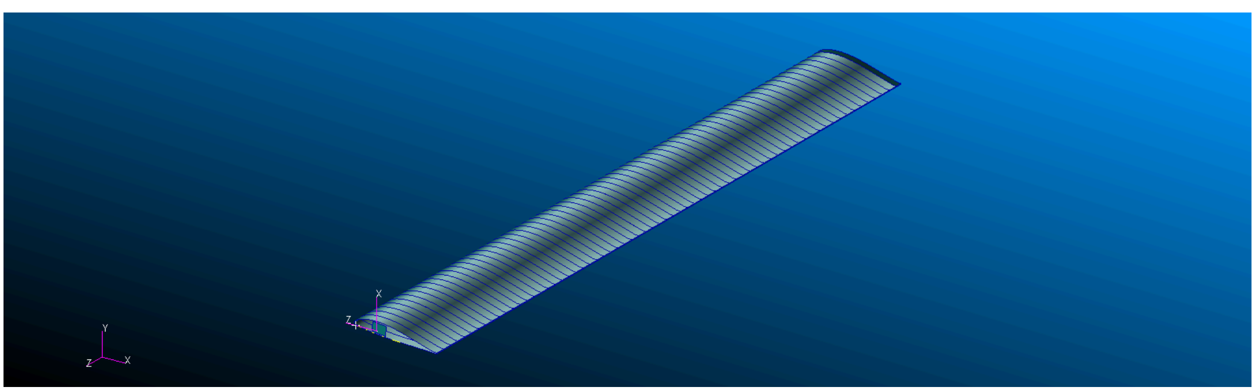

Figure 5: Skin

A surface was also made to close the spar on each end as shown in **Figure 5**.

Strut Geometry:

After the main wing structure was completed, the strut geometry was added. The root strut location was first defined 2.5 ft below the wing root [4.536, 0, 0]. From there, along the direction of the spar, two points at [4.536, 0 . -36] and [4.536, 0 . -72] were made. These two points represented the attachment point of the strut and jury strut.

From these root points, the upper strut attachment points were located relative to the lower surface of the wing. The points were projected onto the lower wing surface using the project function. These projected points were then used to break the rib and skin curves at the correct locations, allowing a strut surface to be created between the lower root points and the wing attachment region.

Jury Strut Geometry:

The jury strut was created using a similar process to the main strut. First, the jury strut attachment point was projected onto the lower surface of the wing. Then, the corresponding curve on the wing was broken at the projected point to create a connection location.
In order to connect the jury strut to the main strut, the main strut curve also had to be broken at the appropriate location. The jury strut surface was then created by connecting the broken curve on the wing/rib region to the broken curve on the main strut. This allowed the jury strut to be modeled as a connected shell component rather than as a disconnected surface.

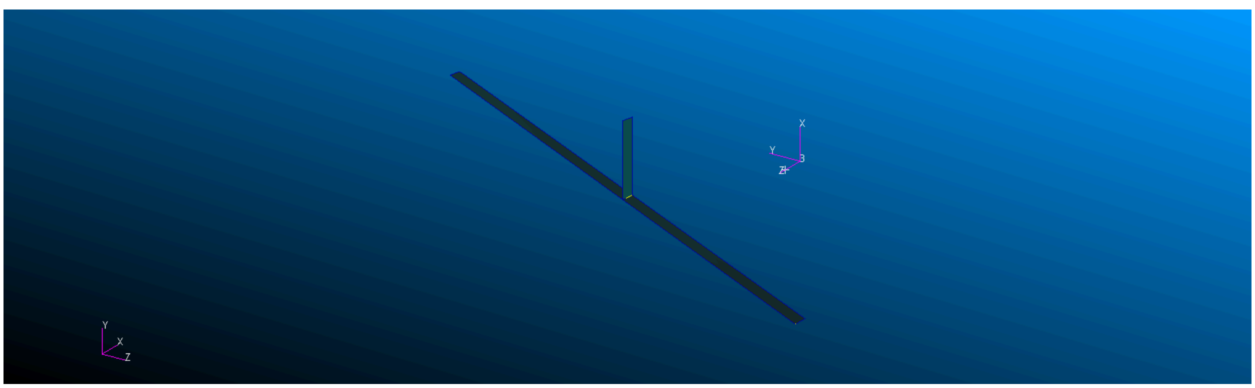

Figure 6: Strut and Jury Strut

Grouping and Property Assignment:

The group function was used throughout the modeling process to separate the ribs, spar, skin, strut, jury strut, and closing surfaces. This organization was important because each component required its own material and 2D shell property assignment.

The shell properties were assigned according to the project requirements. The spar and strut components were assigned the appropriate aluminum properties, while the ribs and other components were assigned their required material properties. Each group was checked to make sure the correct thickness, material, and element property had been applied before running the analysis.

Boundary Conditions and Connectivity:

Boundary conditions were applied after the geometry and shell properties were completed. The root rib was assigned a uniform surface boundary condition to represent the fixed root support. Additional boundary conditions were applied to the spar edges, and the strut was assigned edge boundary conditions at its support location.

Because the ribs and spar were created as separate shell groups, the connectivity between the ribs, spar, skin, and struts had to be carefully defined. During troubleshooting, it was found that if the ribs and spar were not properly connected, only the spar responded significantly during the normal mode analysis. Therefore, boundary and connectivity conditions between the spar and ribs were added or checked so that the full wing structure would participate in the modal response.

Meshing and Normal Mode Analysis:

After the geometry, grouping, properties, and boundary conditions were completed, the model was meshed and prepared for analysis. The Patran model was exported to Nastran for normal mode analysis. The first natural frequencies and corresponding mode shapes were obtained from the Nastran results.

The mode shapes were then viewed in Patran to confirm that the wing skin, ribs, spar, strut, and jury strut were deforming together as a connected structural system. This final check was important to verify that the model behaved as a full wing structure rather than as separate disconnected components.

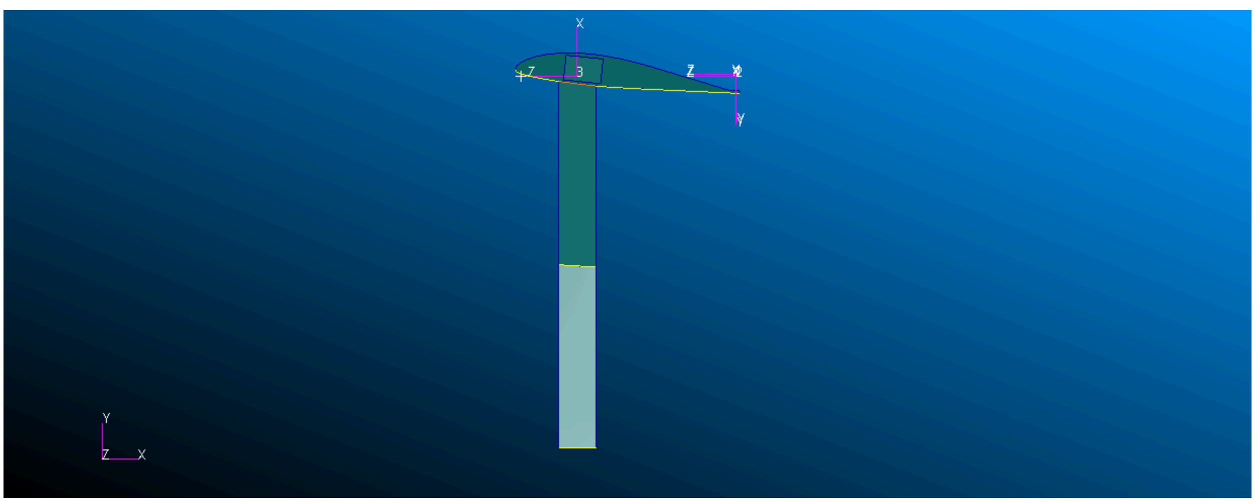

Figure 7: Side View of the Whole Assembly

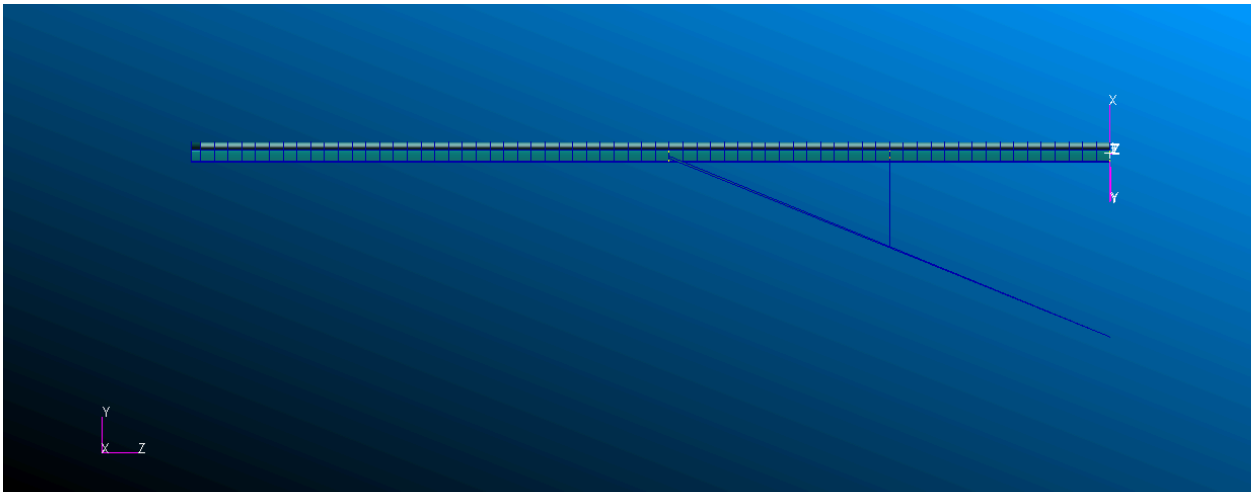

Figure 8: Front View of the Whole Assembly

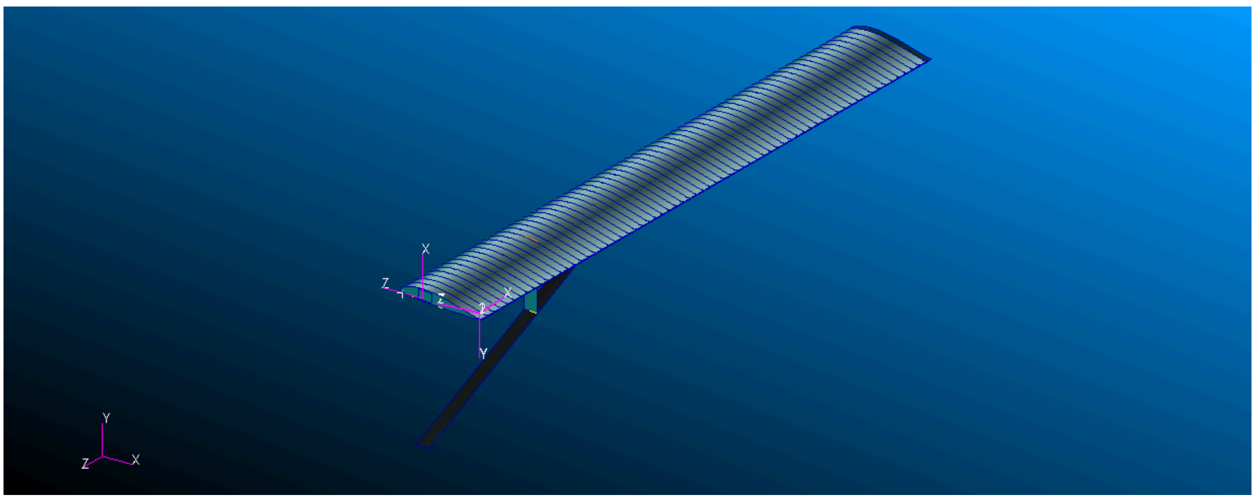

Figure 9: Isometric View of the Whole Assembly from Above

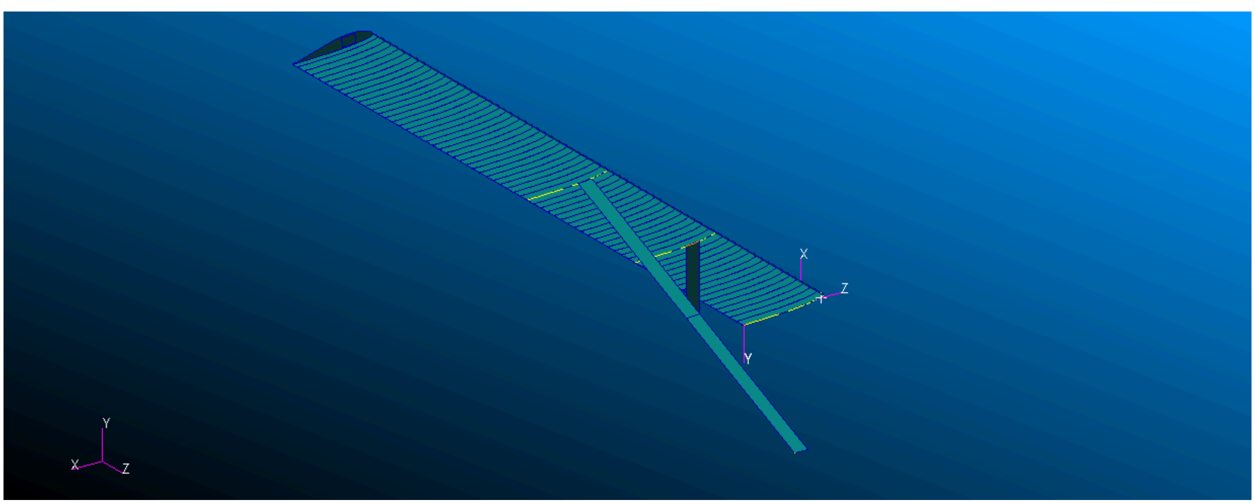

Figure 9: Isometric View of the Whole Assembly from Below

Section 4: Mode Shapes and Natural Frequencies

Simplified 1D Model Results:

The simplified 1D model was solved for the first 15 natural frequencies using the finite axial strut support case. This case was selected as the most realistic simplified model because it did not treat the strut as infinitely stiff. Instead, it represented the main strut as an equivalent vertical spring derived from axial stiffness. The model captured flapwise bending only, so these results are best interpreted as low-order comparison values.

Mode	Simplified 1D Frequency, Hz
1	9.838904
2	64.352388
3	84.637401
4	176.127596
5	217.077752
6	334.552906
7	447.096122
8	595.734249
9	761.666988
10	948.290205
11	1159.529296
12	1387.999493
13	1640.259470
14	1913.906968
15	2203.649358

The first simplified natural frequency was 9.838904 Hz for the finite axial strut support case. The frequency increased compared to the spar-only cantilever case because the strut support increased the effective stiffness of the wing model. The higher modes also increased with mode number, which is expected for beam bending behavior. These results should be compared against the high-fidelity model by looking at mode-shape similarity, not only by matching mode numbers.

High-Fidelity Mode Shapes:

Mode	**High-Fidelity Frequency, Hz**	**Description of Mode Shape**	**Figure**
1	2.487524	First global bending	11, 12
2	3.675869	Spar dominated vertical bending	13, 14
3	5.155889	Spar dominated lateral bending	15, 16
4	5.891264	Global lateral bending	17, 18
5	11.31396	First torsion mode	19, 20
6	13.29240	Coupled higher-order bending with strong strut participation	21, 22
7	17.12338	Higher-order bending/twist	23, 24
8	22.96178	Higher order spar/strut bending	25, 26
9	28.66693	Higher order coupled bending/torsion	27, 28
10	29.87199	Strut dominated higher order coupled mode	29, 30
11	31.33018	Higher order coupled bending/torsion with strut participation	31, 32
12	32.18863	Higher order spar dominated bending	33, 34
13	37.48979	Higher order torsion/coupled wing mode	35, 36
14	38.88275	Higher order bending with minor twist	37, 38
15	46.50964	Higher order coupled	39

		torsion/bending with strong strut participation	

Before final comparison, the high fidelity material densities were checked for consistency with the unit system used in Nastran analysis. The final high fidelity frequencies in the table use mass density values consistent with this unit system.

The high-fidelity modal results showed lower frequencies than the simplified 1D model, but the mode shapes contained structural behavior that the 1D model cannot represent. This was expected because the high-fidelity model included the airfoil geometry, skin, ribs, spar, and strut structure instead of reducing the system to one beam. The simplified model only captures flapwise bending. The higher-fidelity results were therefore better suited for showing local deformation, coupled bending and twisting, and the effect of boundary conditions on the full wing structure. The models were also compared by physical mode character instead of direct mode number matching.

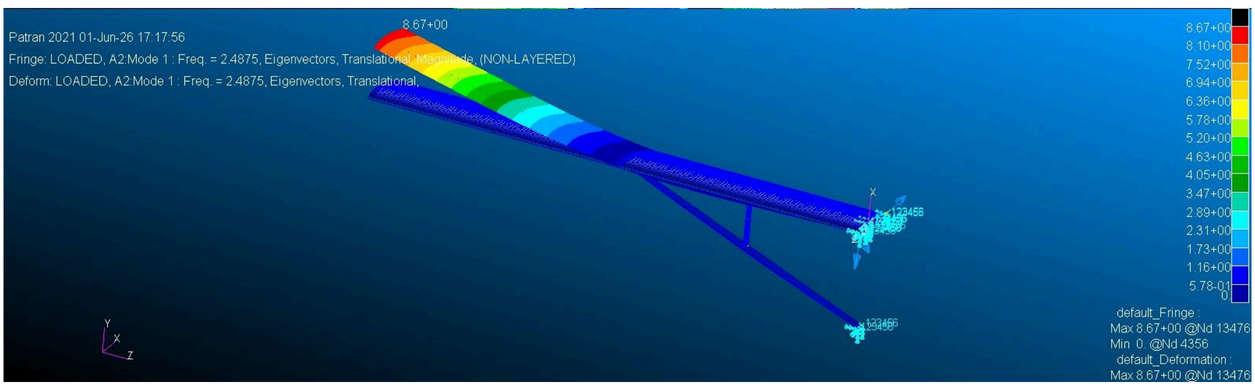

Figure 11: Mode 1 (1st flapwise)

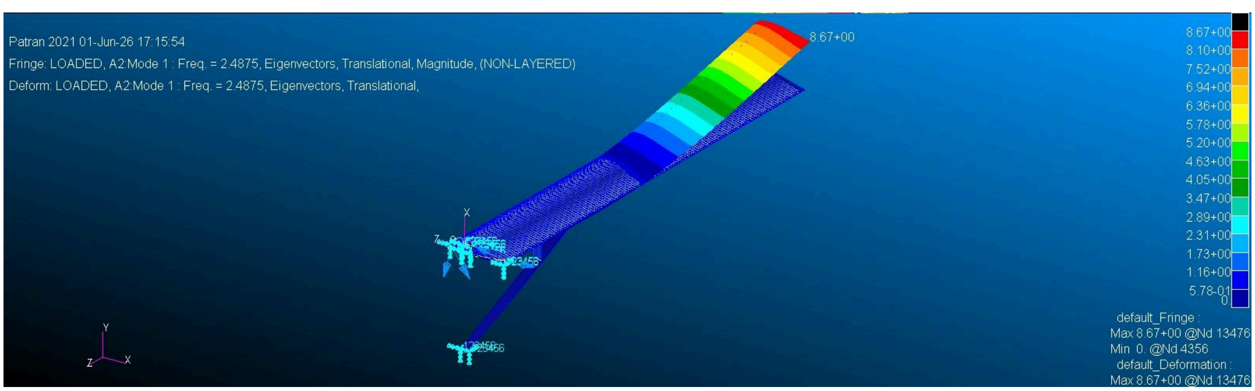

Figure 12: Mode 1 (1st flapwise) Different View

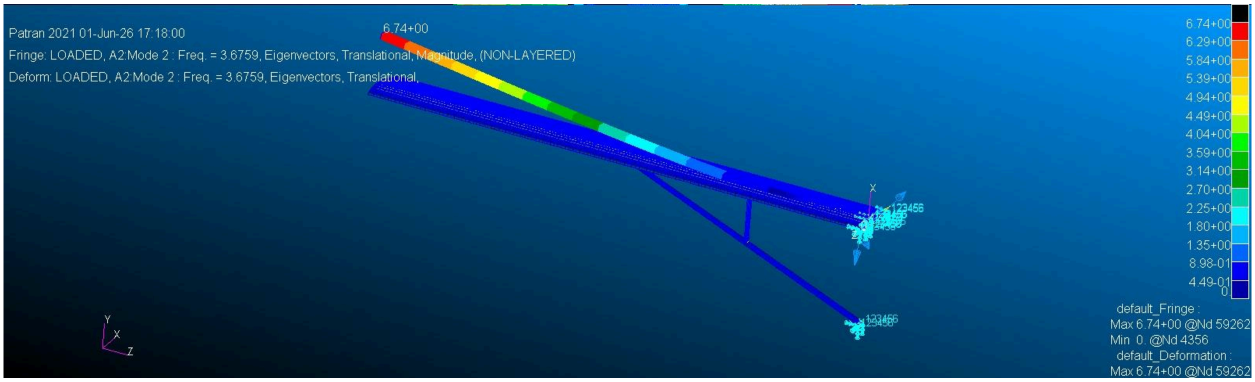

Figure 13: Mode 2

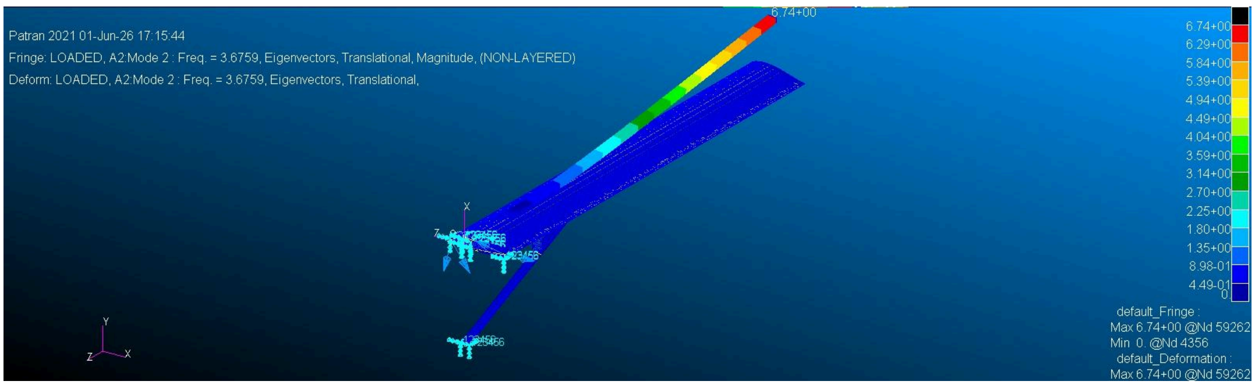

Figure 14: Mode 2 Different View

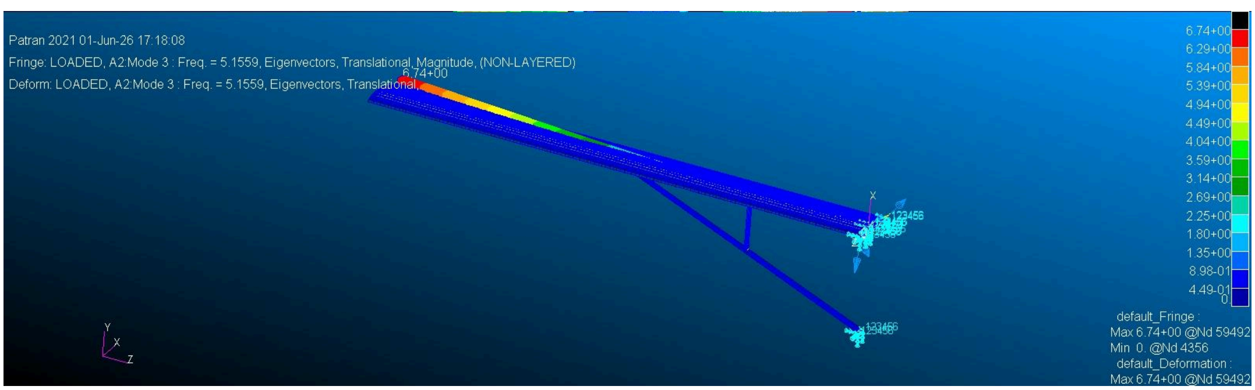

Figure 15: Mode 3

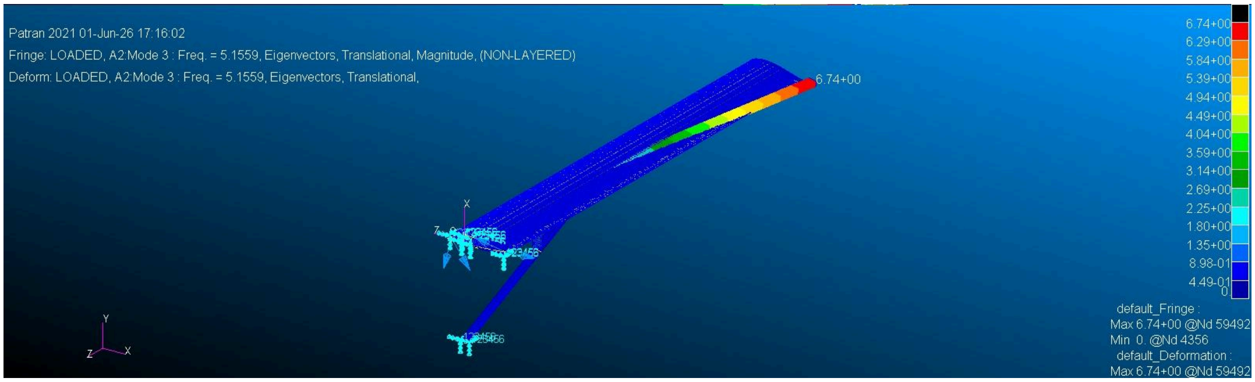

Figure 16: Mode 3 Different View

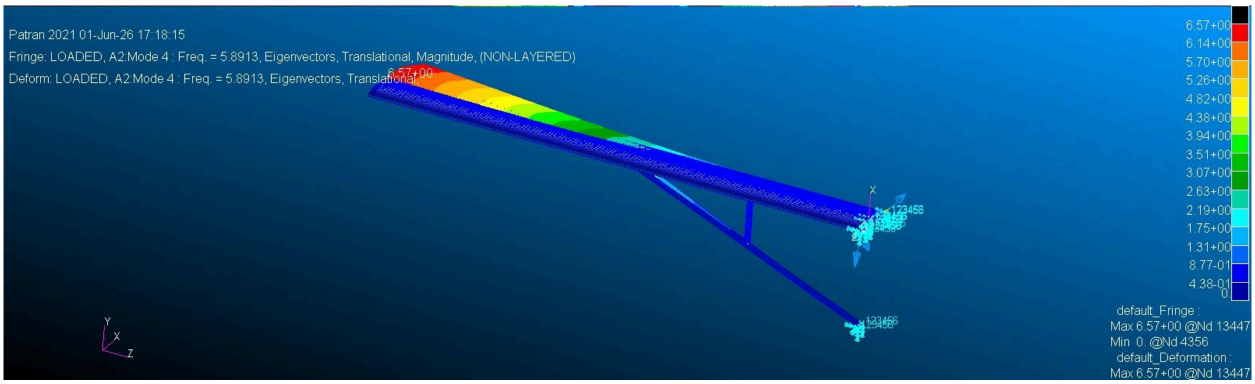

Figure 17: Mode 4

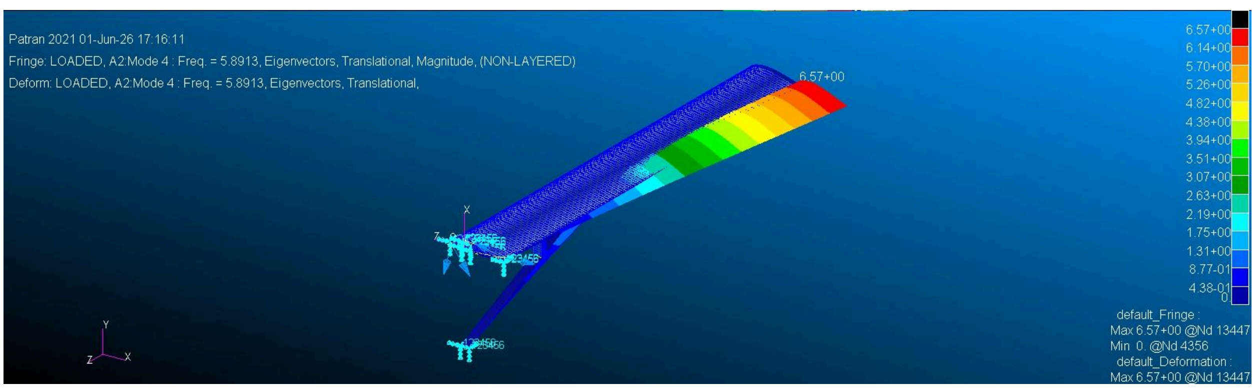

Figure 18: Mode 4 Different View

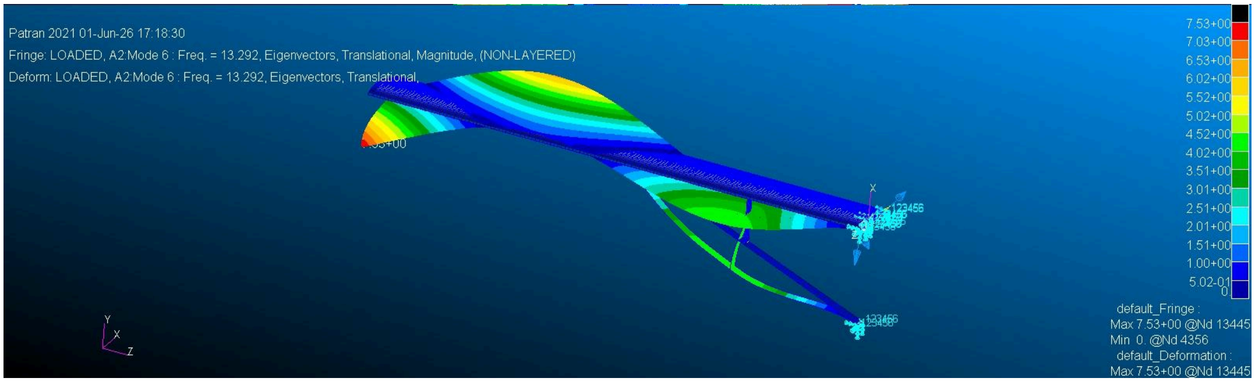

Figure 19: Mode 5

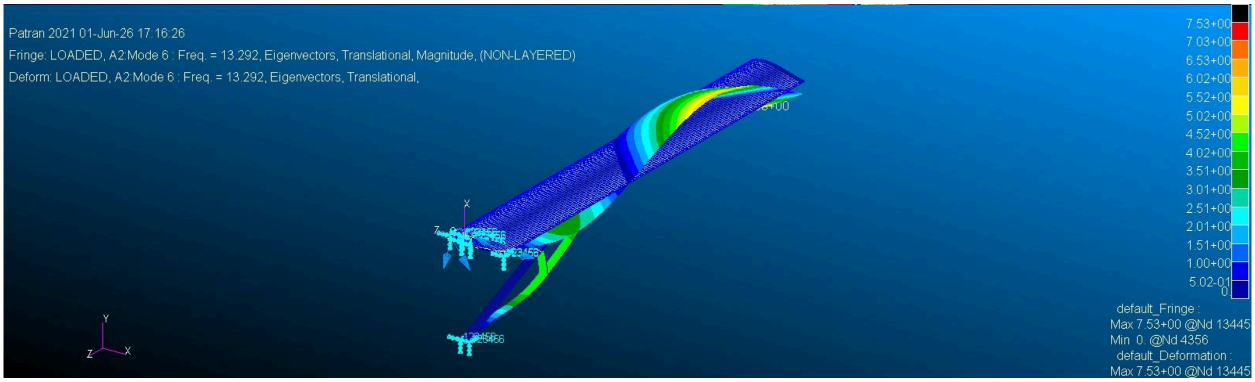

Figure 20: Mode 5 Different View

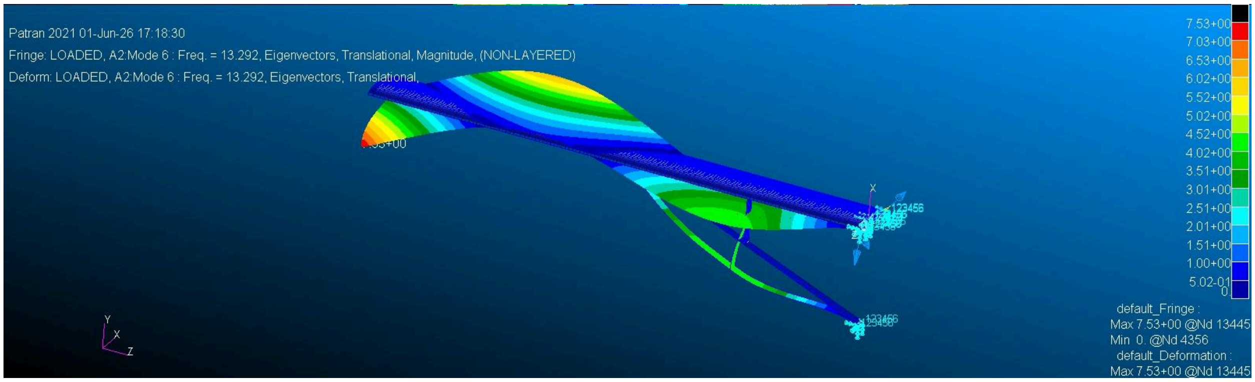

Figure 21: Mode 6

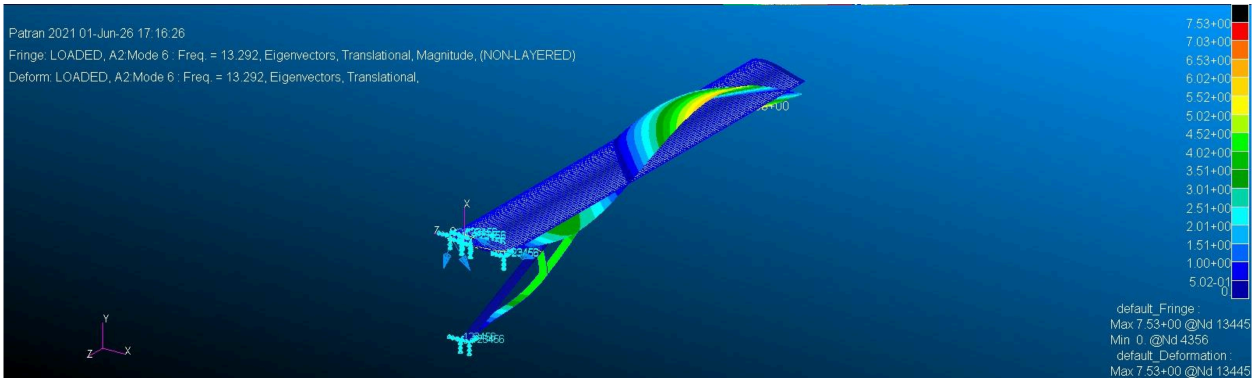

Figure 22: Mode 6 Different View

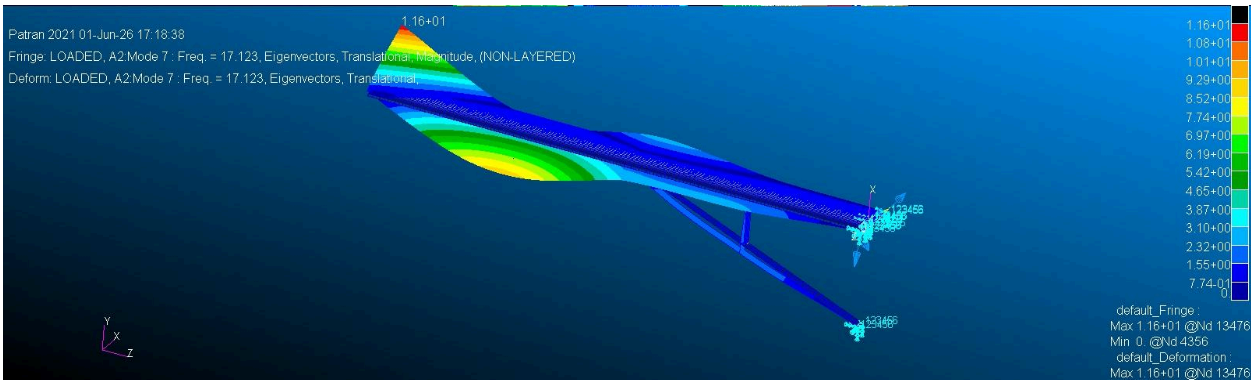

Figure 23: Mode 7

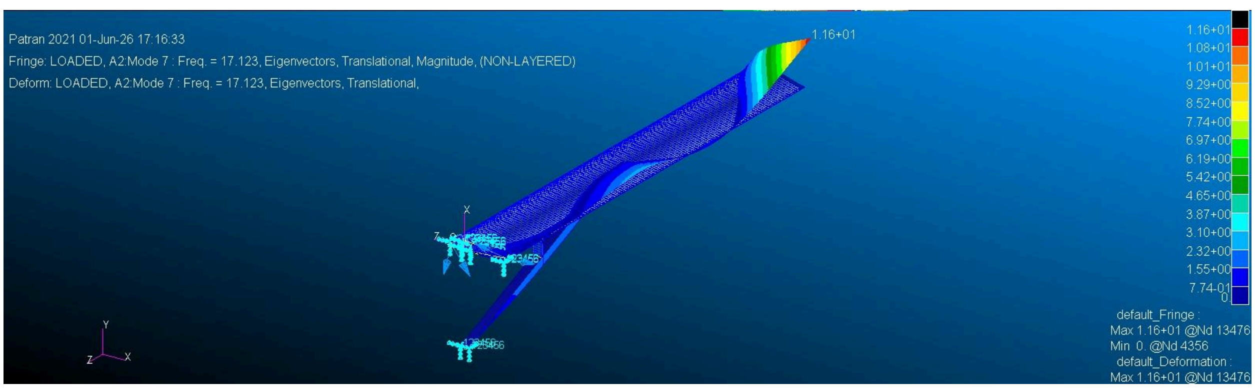

Figure 24: Mode 7 Different View

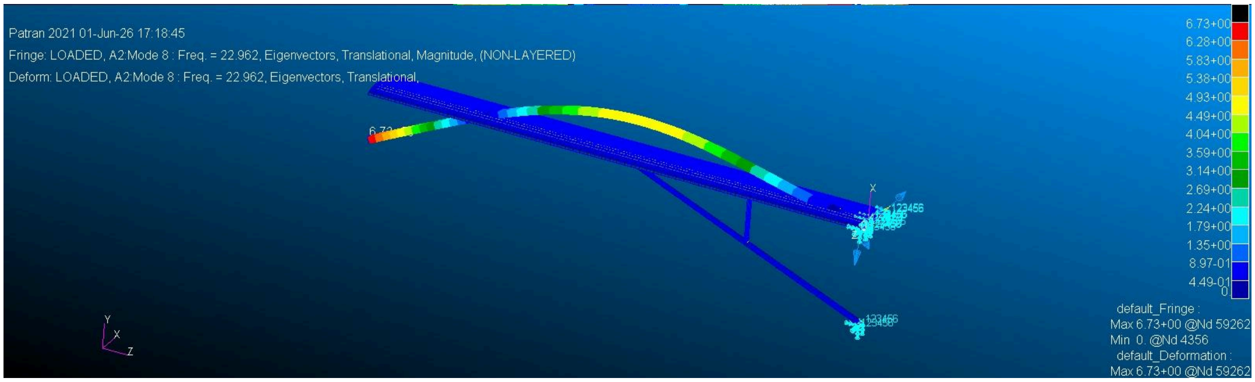

Figure 25: Mode 8

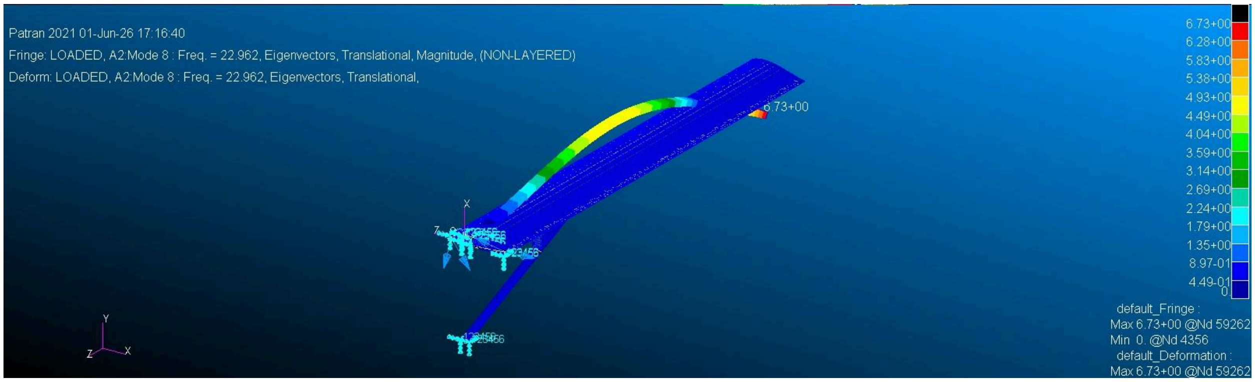

Figure 26: Mode 8 Different View

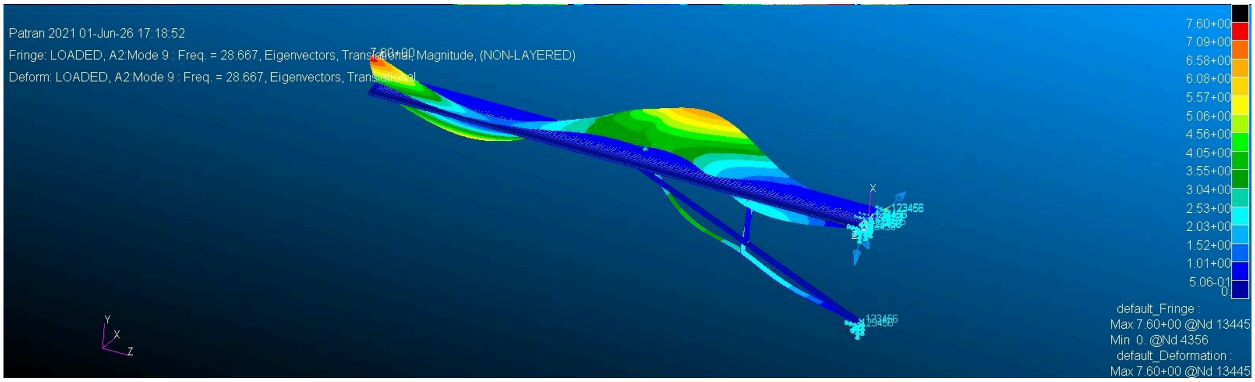

Figure 27: Mode 9

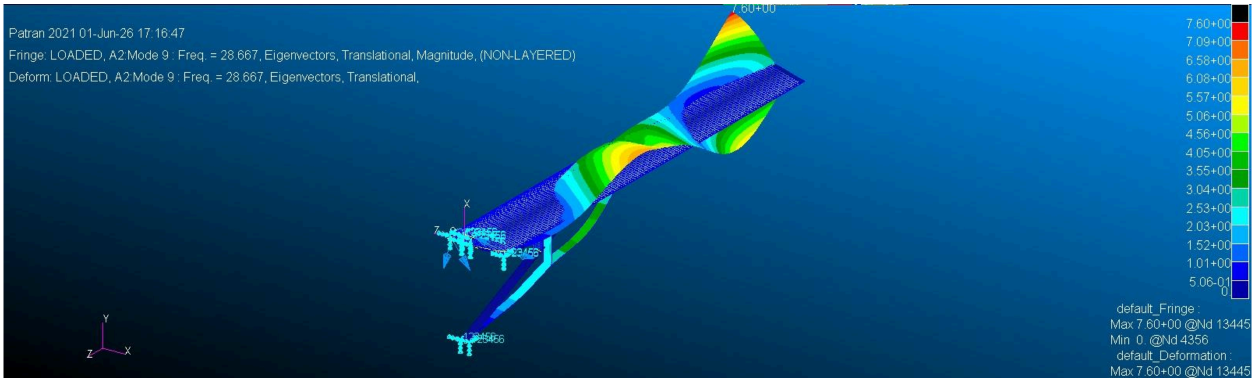

Figure 28: Mode 9 Different View

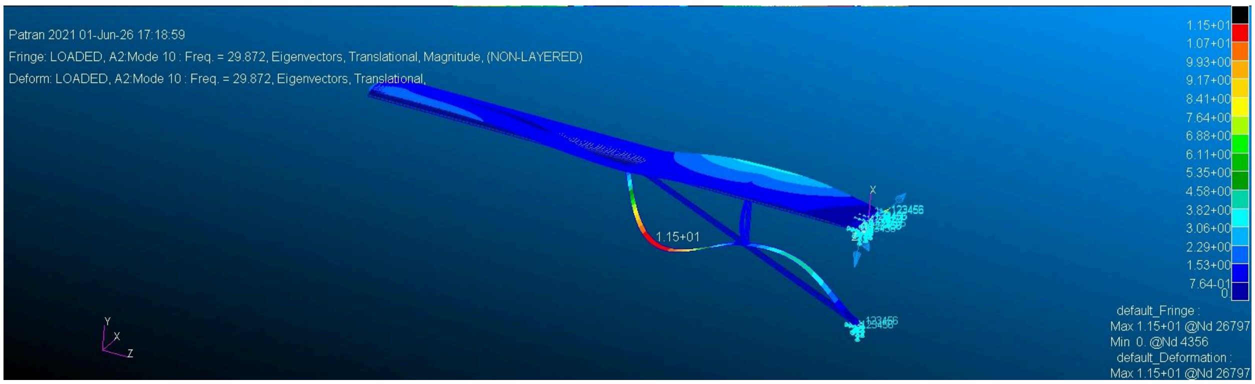

Figure 29: Mode 10

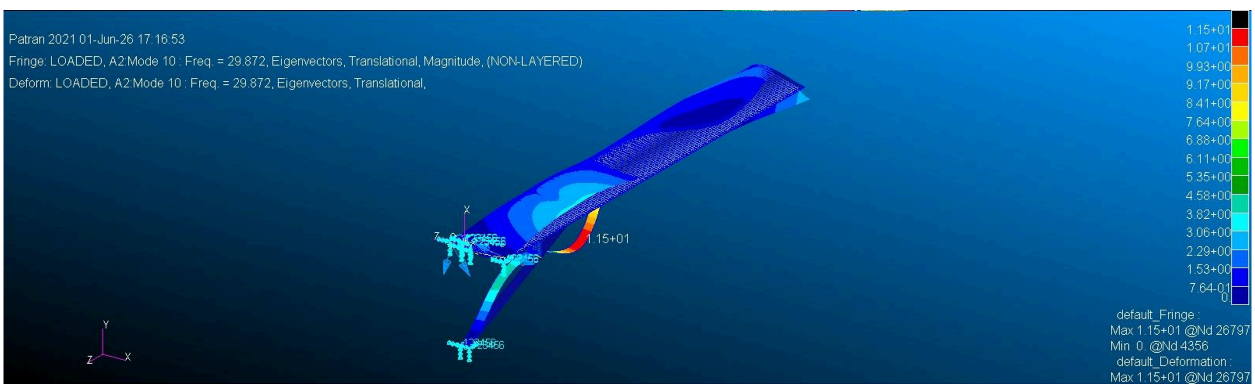

Figure 30: Mode 10 Different View

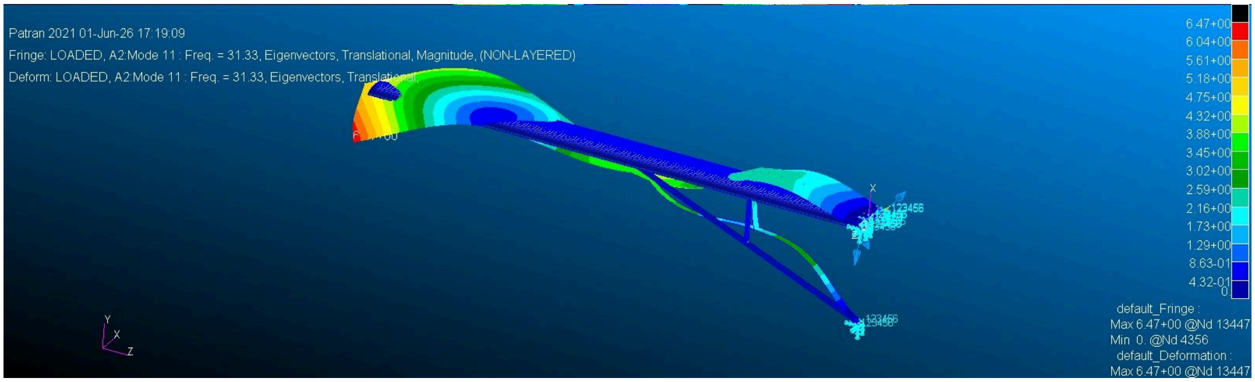

Figure 31: Mode 11

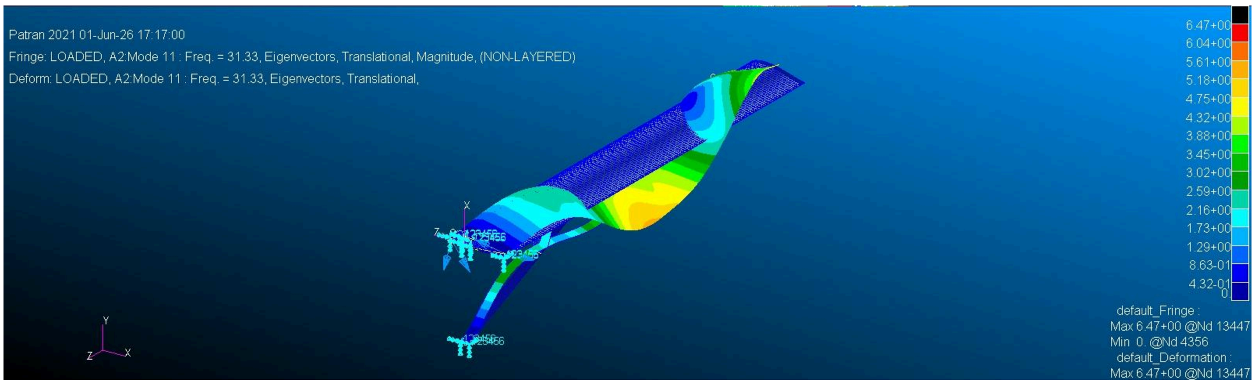

Figure 32: Mode 11 Different View

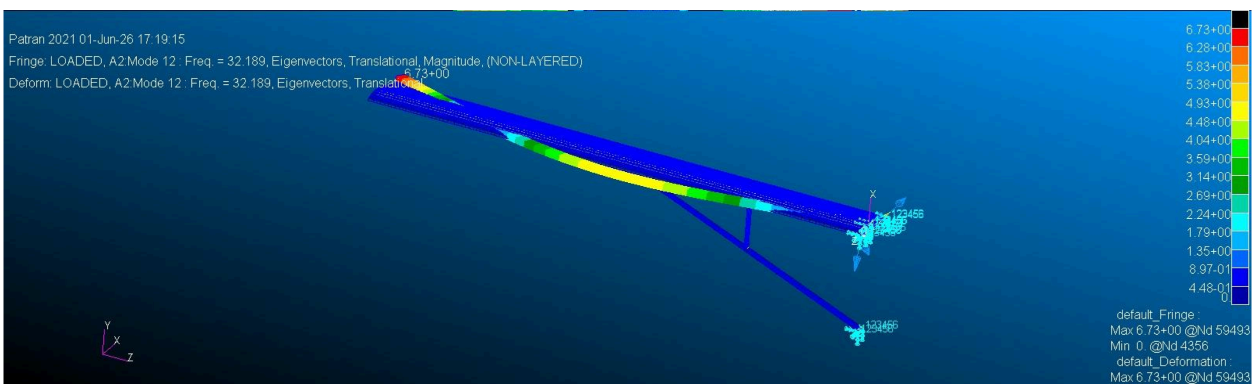

Figure 33: Model 12

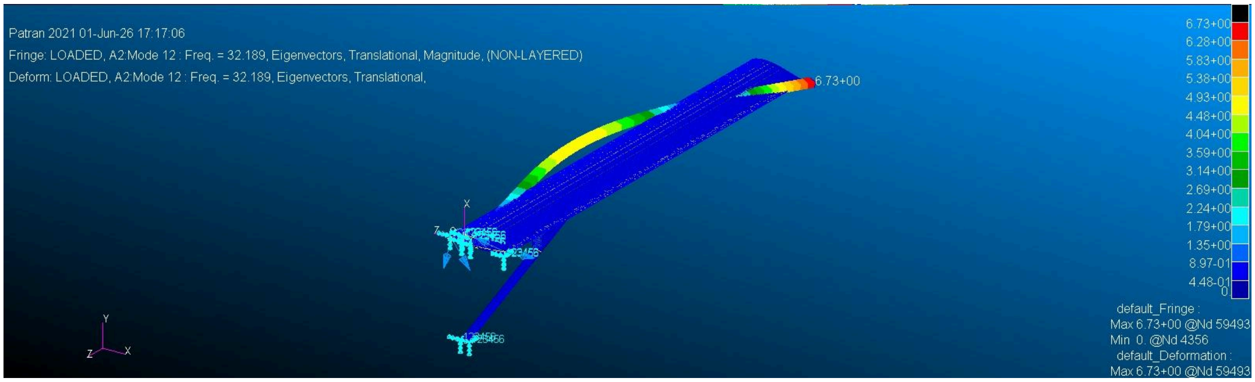

Figure 34: Model 12 Different View

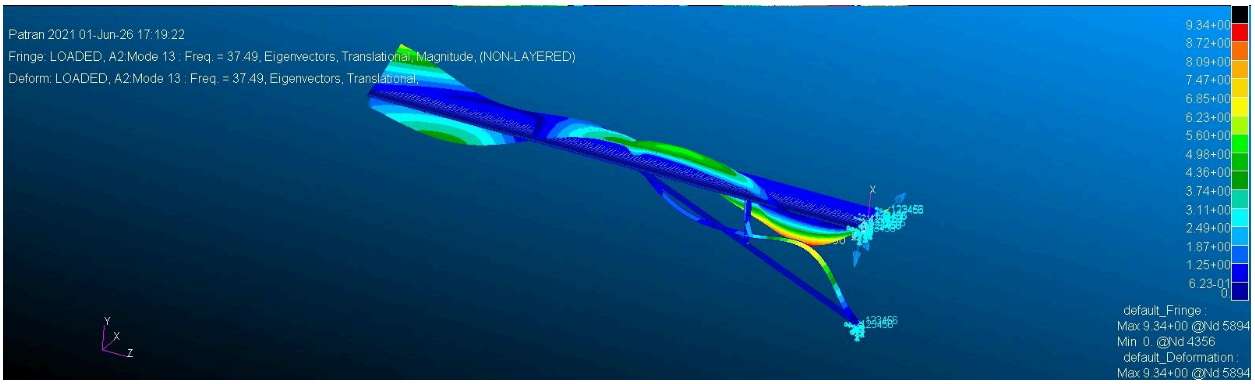

Figure 35: Mode 13

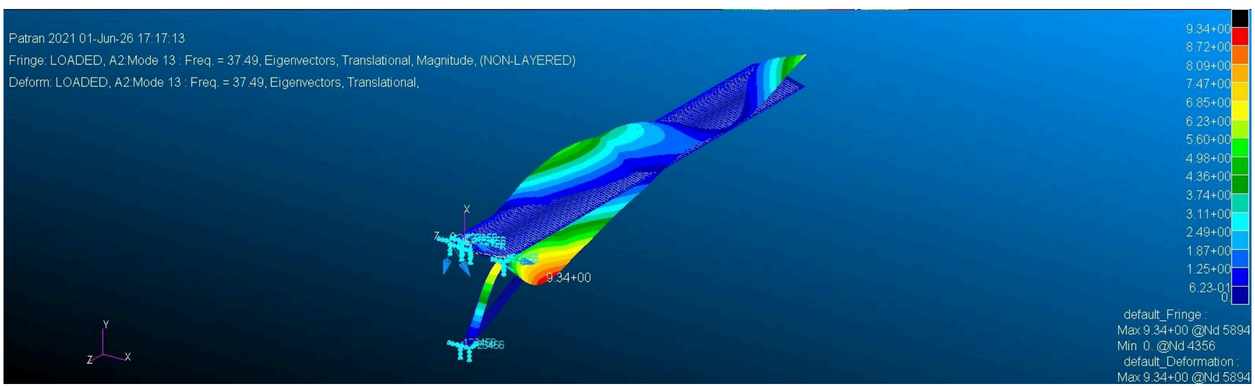

Figure 36: Mode 13 Different View

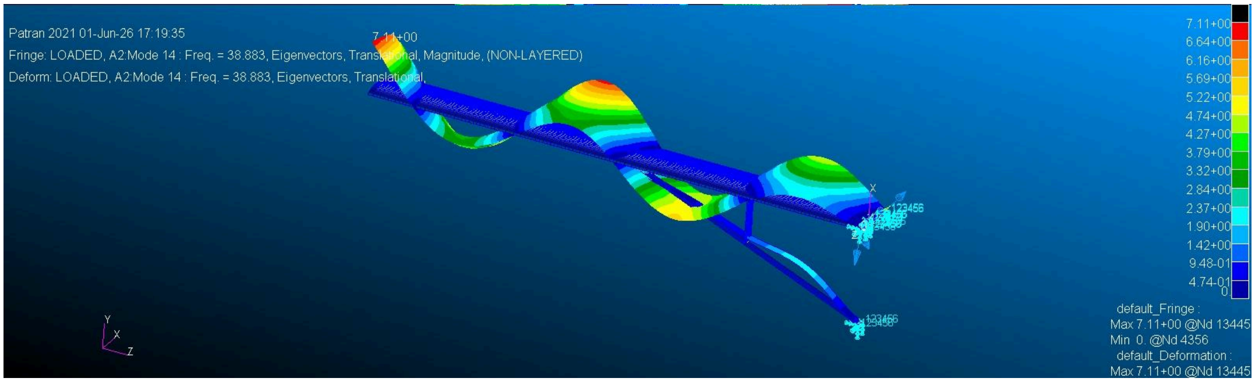

Figure 37: Mode 14

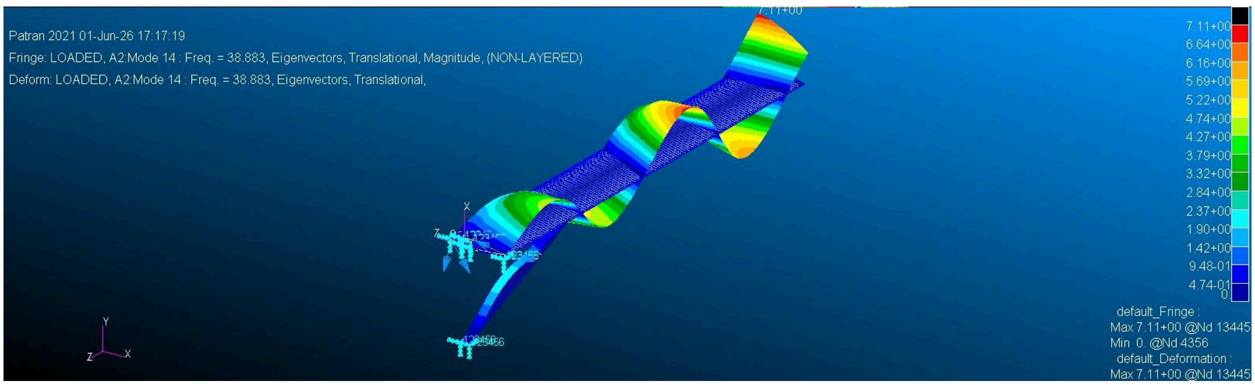

Figure 38: Mode 14 Different View

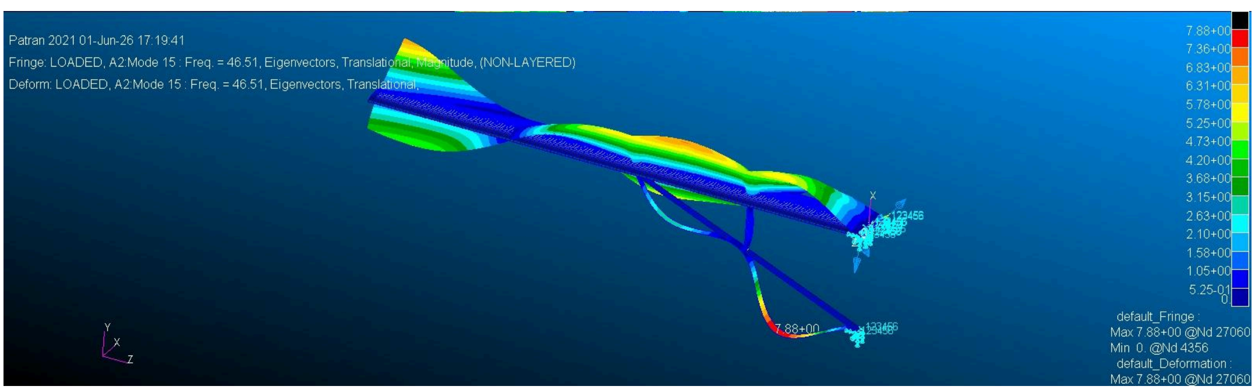

Figure 39: Mode 15

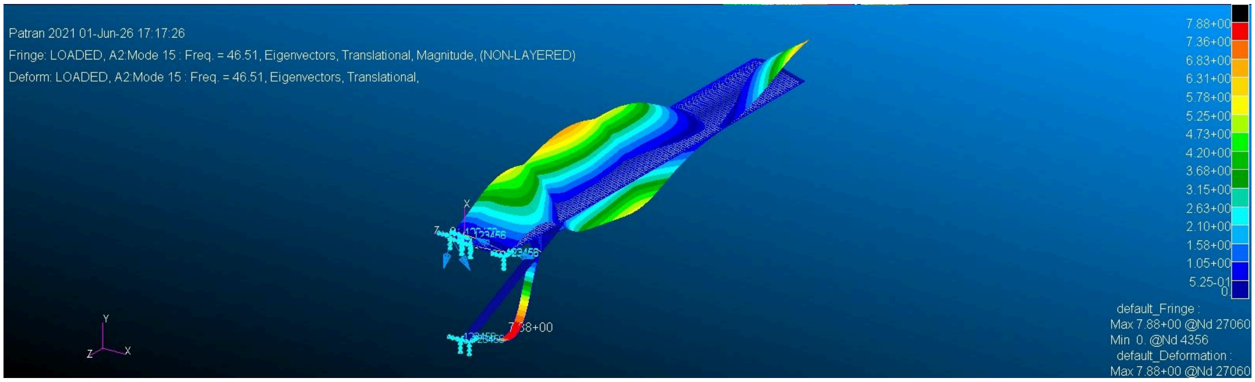

Figure 40: Mode 15 Different View

Section 5: Flutter and Divergence

The project required the team to investigate aeroelastic instability through either divergence or flutter. The main purpose of this section is to connect the modal results to the operating envelope of the aircraft wing. Flutter and divergence are important because they determine whether the wing can remain stable as flow speed increases. The project handout allowed the team to use either a low-order MATLAB model or high-fidelity FlightLoads tools for the instability analysis.

For this project, flutter was selected as the aeroelastic instability to investigate. A low order MATLAB pitch/heave flutter model was used instead of FlightLoads. This model followed the same discriminant based method used in Homework 6, where the two aeroelastic frequency branches are calculated as flow speed increases. Flutter is identified when the two branches coalesce and the discriminant becomes negative.

The structural inputs for the flutter model came from the high-fidelity modal results. Mode 1 was selected as the bending/heave mode because it was the first clear global bending mode of the wing. Mode 5 was selected as the torsion/pitch mode because it was the first clear torsion-like mode. The elastic axis was approximated using the spar centerline at 5.442 inches from the leading edge, and the aerodynamic center was assumed to be at the quarter-chord location. The reduced-order mass parameters were estimated from the corrected high fidelity model.

Flutter Model Input Parameters:

Parameter	**Value**	**Description**
f_h	2.4875 Hz	First global bending mode
f_θ	11.314 Hz	First clear torsion mode
Chord, c	18.14 inches	Wing chord
Semichord, b	9.07 inches	Half chord
Elastic Axis	5.442 inches	Approximated using spar centerline
Aerodynamic Center	4.535 inches	Quarter-chord location

e	0.100	Nondimensional elastic-axis and aerodynamic center offset
μ	40.24	Reduced-order mass ratio
x_θ	0.141	Reduced-order mass center offset
r_θ	0.487	Reduced-order radius of gyration

The baseline flutter results are shown in the table above. Four cases were evaluated. The cases were 6° and 8° angle of attack at sea level and at 20,000 feet. The 20,000 feet case used a density ratio of 0.5328, which increased the effective mass ratio in the reduced-order model.

Baseline Flutter Results:

Case	**AoA**	**Altitude**	**Density Ratio**	μ	**Flutter Speed, (knots)**	**Flutter Frequency, (Hz)**
1	6°	0 ft	1.0000	40.24	117.94	4.9811
2	6°	20,000 ft	0.5328	75.53	161.57	4.9813
3	8°	0 ft	1.0000	40.24	117.94	4.9811
4	8°	20,000 ft	0.5328	75.53	161.57	4.9813

The baseline model predicted flutter speed of 117.94 knots at sea level and 161.57 knots at 20,000 feet. The higher altitude case produced a higher flutter speed because the lower air density reduced the aerodynamic forcing, so a higher flight speed is needed to reach instability. The 6° and 8° angle of attack cases produced the same flutter speed because the linear pitch/heave formulation uses the lift-curve slope $C_{L\alpha}$, but does not explicitly include the trim angle of attack as a separate variable in the flutter discriminant. Therefore, angle of attack was included as a required flight condition, but it did not change the computed flutter boundary in this reduced-order model.

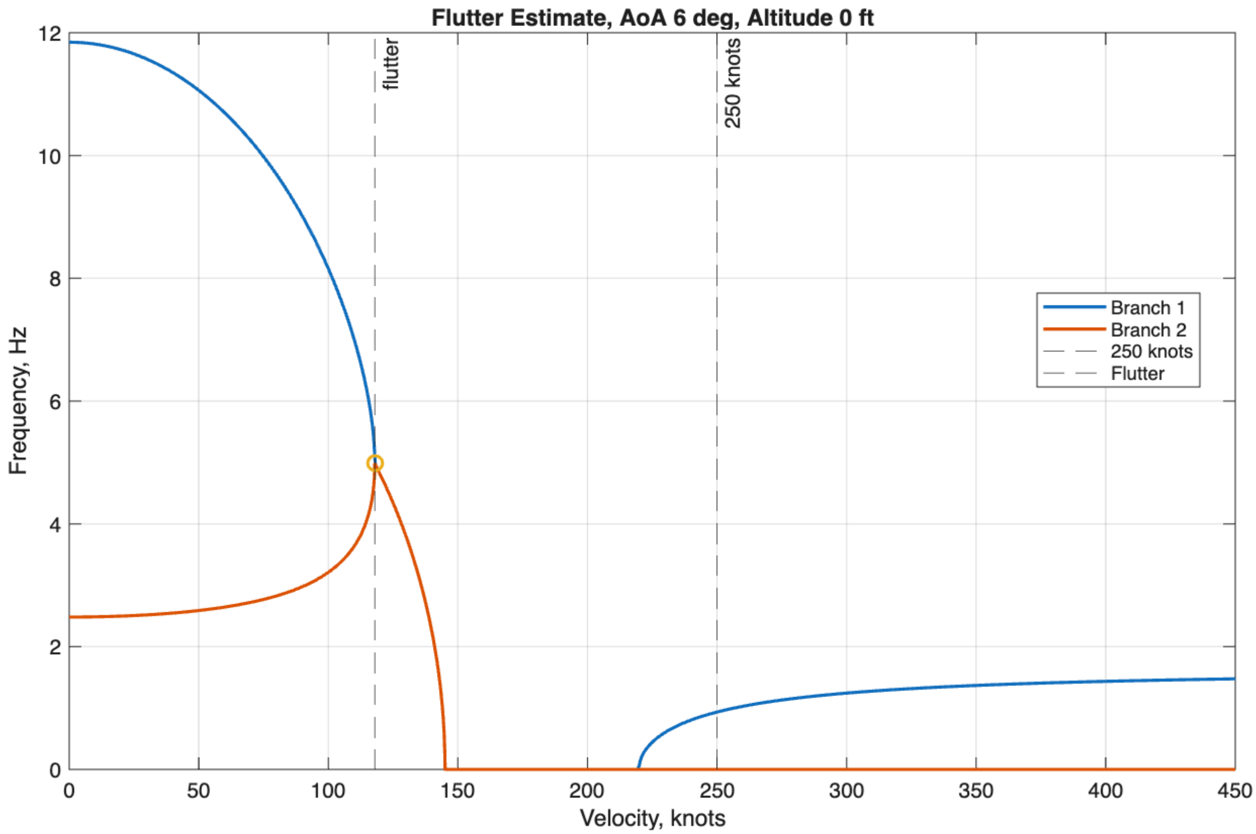

The figure above is the low-order pitch/heave flutter estimate for the sea-level 6° case. The two frequency branches coalesce at approximately 117.94 knots, which is the predicted flutter speed. The 250 knot reference speed is shown for comparison.

A torsion mode sensitivity study was also performed because the high-fidelity model contained several torsion-like and coupled bending/torsion modes. Mode 5 was used as the baseline because it was the first clear torsion-like mode. Higher torsion modes were then tested to show how strongly the flutter result depended on the selected torsional frequency.

Torsion Mode Sensitivity:

Torsion Mode Used	F_θ (Hz)	Flutter Speed (knots)	Flutter Frequency (Hz)
5	11.314	117.94	4.9811
6	13.292	142.83	5.3646
7	17.123	190.96	6.0371
9	28.667	335.73	7.7105
11	31.330	369.12	8.0461
13	37.490	446.29	8.7748

15	46.510	No flutter below 450 knots	N/A

The torsion mode sensitivity study showed that the predicted flutter speed increased as the selected torsional frequency increased. Using mode 5 gave the most conservative result because it was the first torsion mode and produced the lowest flutter speed. Using higher torsion modes moved the predicted flutter speed above the 250 knot reference speed. This shows that the reduced order flutter speed result is highly sensitive to modal selection.

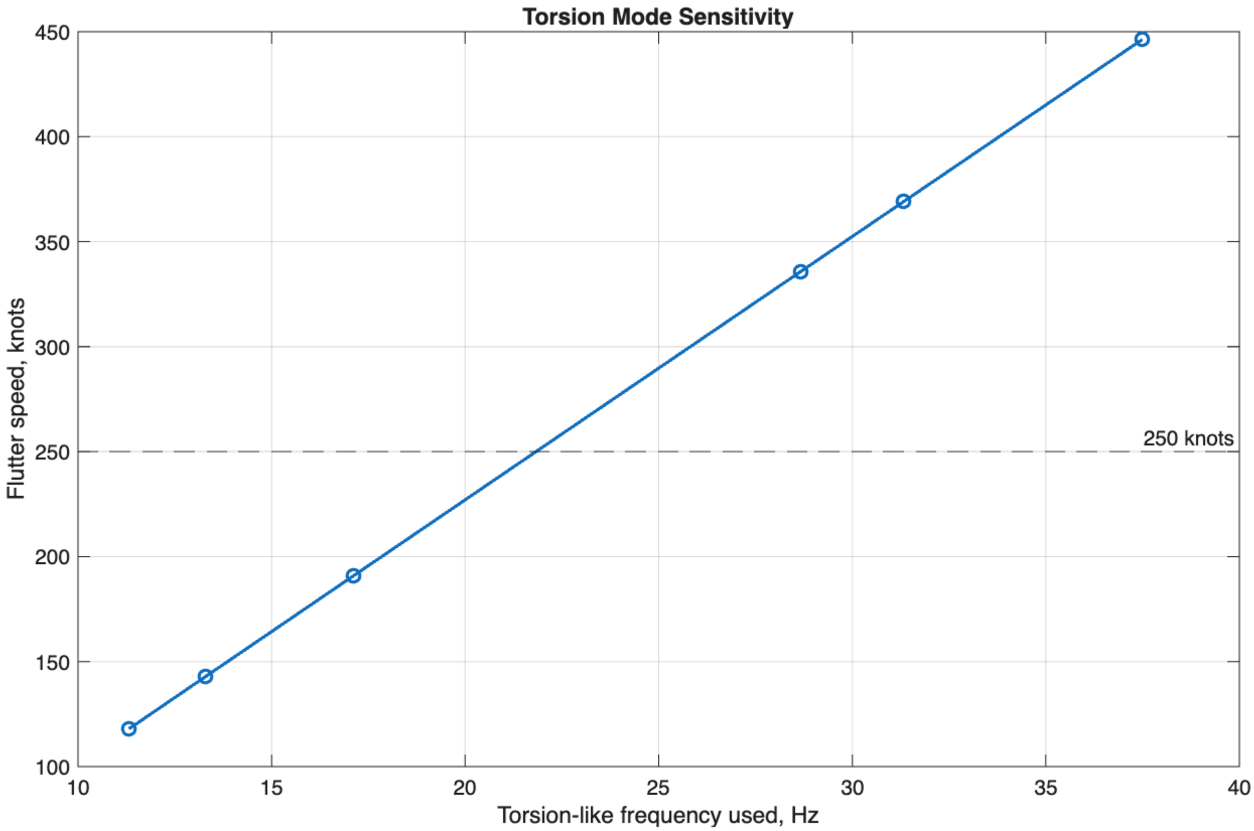

The plot shows sensitivity of predicted flutter speed to the selected torsion mode.Higher torsional frequencies increase the predicted flutter speed, showing that the reduced order flutter result depends strongly on modal selection.

A second sensitivity study was performed on the reduced-order mass and inertia parameters mu x_θ and r_θ. These values were estimated from the high-fidelity model, but they are still approximate because the full truss braced wing is being reduced into a two degree-of-freedom pitch/heave model. Across the tested values, the predicted sea-level flutter speed ranged from approximately 117.94 knots to 255.87 knots. Increasing r_θ and μ generally increased the predicted flutter speed. This confirms that the baseline result should be interpreted as a conservative low-order estimate rather than a final validated flutter boundary.

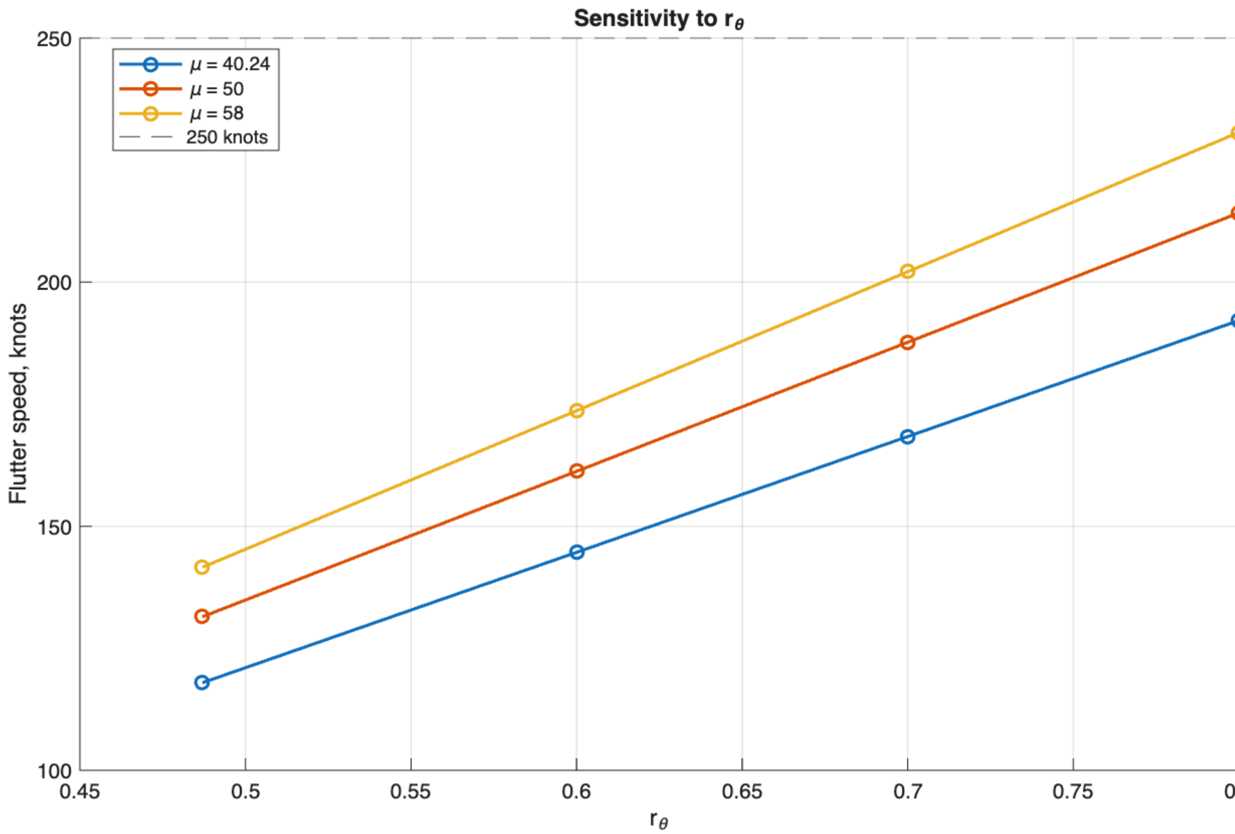

This plot shows the sensitivity of predicted flutter speed to r_θ and μ. The result changes noticeably with reduced order inertia assumptions.

Overall, the low order flutter model predicted flutter below the 250 knot operating speed for the conservative baseline case. However, the sensitivity studies showed that the result depends strongly on torsional mode selection and reduced order inertia assumptions. Therefore, the result should be treated as a preliminary flutter estimate rather than a final aeroelastic prediction.

Section 6: Interpretation of Results

The simplified 1D model and high-fidelity Patran/Nastran model served different purposes. The simplified model was useful because it gave a quick and understandable estimate of the wing's flapwise bending frequencies. It also made it easier to see how the main strut increased the stiffness of the system. However, the simplified model cannot represent the full 3D behavior of the wing, so it should not be treated as the final prediction.

The high-fidelity model was more realistic because it included the airfoil geometry, spar, ribs, skin, and strut structure. This model was better for showing the true deformation pattern of the wing and capturing behavior that the 1D model cannot show. At the same time, the high-fidelity model was more sensitive to modeling details. Mesh quality, material density, and boundary condition selection had a major effect on whether the analysis ran properly and whether the results were usable.

The most important result from the simplified model was that adding strut stiffness increased the first natural frequency compared to the spar-only case. This makes physical sense because the strut reduces the effective flexibility of the wing. In the high-fidelity model, the mode shapes showed that the wing response was not just simple beam bending. The full model included bending, twisting, and local structural behavior, which explains why direct mode-number matching between the simplified and high-fidelity models is not always enough. The better comparison is based on whether the shapes of the modes are physically similar.

Section 7: Lessons Learned

Ivan Leung:

Through this project, I learned how useful simplified models can be when starting a complicated aeroelastic problem. The 1D beam model was not perfect, but it helped me understand the basic stiffness and frequency trends before comparing against the high-fidelity model. I also learned that assumptions need to be written clearly because small modeling choices, such as spar orientation, strut stiffness, and mass distribution, can change how the results should be interpreted.

Jacob George:

Through this project, I learned more about how low-order and high-fidelity models connect to each other. The simplified model helped provide a baseline, while the higher-fidelity work showed how much more complicated the real structure becomes once geometry, mesh, and boundary conditions are included. I also learned that getting results is only part of the project; understanding whether the model setup makes physical sense is just as important.

Elian Castillo:

Through this project, I learned how sensitive finite element results can be to boundary conditions and modeling details. Even when the geometry looks correct, the model may not behave correctly if the constraints, mesh, or material definitions are not set up properly. This helped me better understand why verification and troubleshooting are important parts of engineering analysis.

Kaitaro Hori:

Through this project, I learned that building a high-fidelity model takes a lot of iteration. Creating the geometry, meshing the ribs and skin, and getting the analysis to run required more troubleshooting than expected. The project helped me understand that high-fidelity models can give more realistic results, but they also require careful setup and patience.

Anthony Damian:

Through this project, I learned how material properties, density, boundary conditions, and meshing all affect finite element results. One of the biggest takeaways was that a model can appear complete visually but still fail or give incomplete results if the analysis setup is missing something important. This project helped me better understand the connection between class concepts and real modeling issues.

Section 8: Team Member Contributions

Team Member	Contribution
Ivan Leung	Developed the simplified 1D MATLAB model, documented assumptions, calculated simplified natural frequencies, helped organize the slides/report structure, and supported comparison between simplified and high-fidelity results.
Jacob George	Developed the low-order/Patran model and helped produce modal results for comparison. Also helped with slide content and presentation planning.
Elian Castillo	Helped with model validation, interpretation of frequency and mode-shape behavior, and review of the high-fidelity model setup.
Kaitaro Hori	Worked on high-fidelity Patran model development, including geometry, meshing, and troubleshooting of the wing, ribs, and skin model.
Anthony Damian	Helped troubleshoot the high-fidelity Patran/Nastran setup, including material density, boundary conditions, and successful modal result generation. Also helped with video editing and presentation organization.

References

[1] Professor Sarigul-Klijn and the EME 139 Teaching Team. EME 139 Team Term Paper Final Report Guide. University of California, Davis, 2026.

[2] Professor Sarigul-Klijn and the EME 139 Teaching Team. Dynamic System for Instability Predictions: A Truss-Braced Aircraft Wing. University of California, Davis, 2026.

[3] MSC Software. Patran/Nastran finite element analysis software, Version 2021.

[4] MATLAB. MATLAB numerical computing environment, The MathWorks.

Appendix

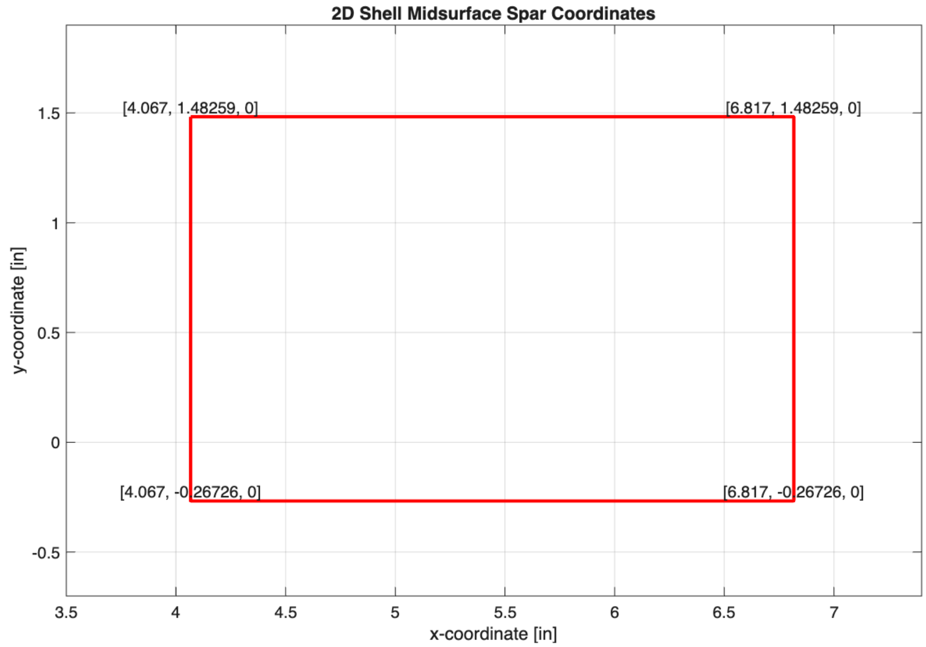

Figure 1A: Coordinates for the Midline of the Spar Cross Section

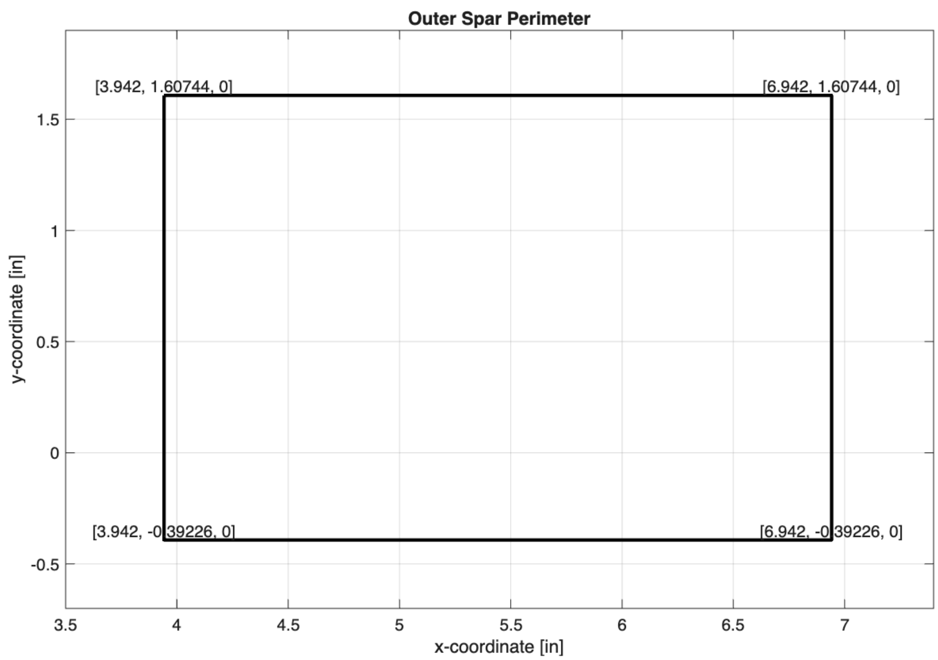

Figure 2A: Coordinates for the Outer Perimeter of the Spar Cross Section